A Realistic Breast Phantom Proposal for 3D Image Reconstruction in Digital Breast Tomosynthesis

Adem Polat, PhD[1] (ID) **and Raziye Kubra Kumrular, MSc**[2] (ID)

Abstract

Objectives: Iterative (eg, simultaneous algebraic reconstruction technique [SART]) and analytical (eg, filtered back projection [FBP]) image reconstruction techniques have been suggested to provide adequate three-dimensional (3D) images of the breast for capturing microcalcifications in digital breast tomosynthesis (DBT). To decide on the reconstruction method in clinical DBT, it must first be tested in a simulation resembling the real clinical environment. The purpose of this study is to introduce a 3D realistic breast phantom for determining the reconstruction method in clinical applications. **Methods:** We designed a 3D realistic breast phantom with varying dimensions (64^3-512^3) mimicking some structures of a real breast such as milk ducts, lobules, and ribs using TomoPhantom software. We generated microcalcifications, which mimic cancerous cells, with a separate MATLAB code and embedded them into the phantom for testing and benchmark studies in DBT. To validate the characterization of the phantom, we tested the distinguishability of microcalcifications by performing 3D image reconstruction methods (SART and FBP) using Laboratory of Computer Vision (LAVI) open-source reconstruction toolbox. **Results:** The creation times of the proposed realistic breast phantom were seconds of 2.5916, 8.4626, 57.6858, and 472.1734 for 64^3, 128^3, 256^3, and 512^3, respectively. We presented reconstructed images and quantitative results of the phantom for SART (1-2-4-8 iterations) and FBP, with 11 to 23 projections. We determined qualitatively and quantitatively that SART (2-4 iter.) yields better results than FBP. For example, for 23 projections, the contrast-to-noise ratio (CNR) values of SART (2 iter.) and FBP were 2.871 and 0.497, respectively. **Conclusions:** We created a computationally efficient realistic breast phantom that is eligible for reconstruction and includes anatomical structures and microcalcifications, successfully. By proposing this breast phantom, we provided the opportunity to test which reconstruction methods can be used in clinical applications vary according to various parameters such as the No. of iterations and projections in DBT.

Introduction

Microcalcifications within the breast are present in approximately 30% of malignant lesions and masses, and they are important indicators of early breast cancer.[1,2] Microcalcifications expressing calcifications smaller than 1 mm in diameter can be detected utilizing digital breast tomosynthesis (DBT) mammography modality with a resolution of less than 100 μm.[1] DBT, which is an advanced

[1] Department of Electrical-Electronics Engineering, Çanakkale Onsekiz Mart University, Çanakkale, Turkey
[2] Institute of Sound and Vibration Research, University of Southampton, Southampton, UK

Corresponding Author:
Adem Polat, Department of Electrical-Electronics Engineering, Çanakkale Onsekiz Mart University, Çanakkale 17100, Turkey.
Email: adempolat@comu.edu.tr

form of x-ray mammography evolved by Gershon-Cohen, Leborgne, and others, is one modality being developed to detect lesions, masses, and microcalcifications in a breast.[3–7] Analytical and iterative algorithms have been used for reconstructing three-dimensional (3D) images slice by slice to detect distortions, masses, lesions, and microcalcifications in each slice in DBT. Iterative algorithms such as the algebraic reconstruction technique (ART) introduced by[8] and the simultaneous ART (SART) introduced by[9] have been used as new alternative methods for analytical image reconstruction techniques such as filtered back projection (FBP) which was first advanced by Bracewell and Riddle[10] and later independently by Ramachandran and Lakshminarayanan[11] to reconstruct 3D images of a breast.[12] Shepp and Logan demonstrated the superiority of FBP over algebraic reconstruction methods in 1974.[13] However, FBP requires a full scan of the target to provide a better image, while algebraic reconstruction methods do not. For example, with SART, a 3D image of the breast can be created with only a few projections, usually ranging from 9 to 25,[5] obtained from a limited viewing angle scan of the breast that causes incomplete data.[5,14] FBP algorithm is based on the inverse Radon transform,[15] while the SART algorithm yields a solution discretizing the Radon transform for a linear algebraic system iteratively.[16] Due to the FBP requires complete projection data, the results of reconstruction provide less accuracy because of using incomplete projection data in DBT. Compared with the FBP, the main advantage of SART is that it is opportune to apply to incomplete and noisy projections in DBT.[16–21]

A large No. of projections are required for the FBP to provide a successful image reconstruction in DBT. However, as a high No. of projections will cause high doses of radiation and this carries the risk of cancer even in a healthy breast, it becomes necessary to view with a limited No. of projections. SART provides a considerable superior over FBP in terms of high-quality image reconstruction using a few No. of projections taken in a narrow angle range. Regardless of the image reconstruction method, comprehensive analyses of the proposed method should be performed in a simulation environment before applying it in clinical DBT in terms of cost, duration, and radiation risk. Some software tools such as the open-source DBT reconstruction toolbox developed at Laboratory of Computer Vision (LAVI), Research group at University of São Paulo (USP),[22,23] open virtual clinical trials (OpenVCT),[24–26] and The All Scale Tomographic Reconstruction Antwerp (ASTRA) toolbox generated by the collaboration of Antwerp University, Belgium, and the Centrum Wiskunde Informatica, Amsterdam, The Netherlands[27,28] have been introduced for 3D image reconstructions in medical imaging such as tomography and DBT. ASTRA offers reconstruction ability for tomographic applications such as computed tomography (CT) and electron tomography, while open-source DBT reconstruction toolbox by LAVI (we will henceforth refer to as the LAVI) provides a software environment that mimics a realistic implementation of clinical DBT. LAVI offers several reconstruction methods such as FBP, SART, simultaneous iterative reconstruction technique (SIRT), and maximum likelihood expectation maximization (MLEM).

On the other hand, recently, several open-source software packages such as XDesign,[29] TomoPy,[30] syris,[31] and TomoPhantom[32] have been released that provide the generation of the analytical phantoms mainly based on application to x-ray-based image reconstructions. TomoPhantom, which was written in the C-OpenMP language providing wrappers for Python and MATLAB supports 2D objects, including circles, ellipses, rectangles, and parabolas and enables computationally efficient generation of 2D-4D high-resolution phantoms. In literature, there are a few existing studies about digital breast phantoms. These studies have some limitations such as computation time cost (2 h 32 min)[33] and applying only FBP as a reconstruction method.[34]

In this paper, we present a realistic breast phantom mimicking the main structures of a real breast including nodules, milk ducts, lesions, masses, and microcalcifications using the TomoPhantom software package for testing and benchmark studies in DBT. The proposed phantom enables a variety of dimensions with $64 \times 64 \times 64$ (64^3), $128 \times 128 \times 128$ (128^3), $256 \times 256 \times 256$ (256^3), and $512 \times 512 \times 512$ (512^3) which can be used to rigorously evaluate image reconstruction algorithms. Another advantage of this phantom is computational efficiency compared to other digital breast phantoms. The creating time of our proposed realistic breast phantom was a maximum of 8 min for maximum dimension of 512^3. We also performed various reconstruction methods such as FBP and SART (with 1-2-4-8 iterations). To validate the characterization of our proposed realistic breast phantom, we tested the visibility of the structures and especially the distinguishability of the microcalcifications that mimic cancerous cells in the breast using the reconstruction tool of LAVI.

Materials and Methods

Traditionally, the FBP algorithm, which performs a filtering operation on the projections before backprojection using a ramp filter as a high-pass filter and the Hann filter as a windowing technique, is used for DBT reconstruction.[26,34] FBP uses the mathematical fundamentals of Radon transform and Fourier transform,[15] on the other hand, SART is based on solving a linear algebraic equation system. These reconstruction algorithms are generally tested on the simplistic numerical phantoms, which do not appropriate for DBT imaging applications. The aim of this study is (1) to introduce a realistic breast phantom that is computationally efficient and (2) to validate that the phantom mimics the real breast characterization by applying FBP and SART. Details of the phantom design and SART are explained in the next subsection.

Realistic Breast Phantom Design

Breast phantoms are numerical or physical models of the breast developed to evaluate and improve the image quality of breast imaging systems. Simulation environments are of undeniable importance for the development and testing of 3D image reconstruction methods used in clinical DBT applied by giving

radiation to patients. TomoPhantom includes various geometric objects such as ellipses, cuboids, rectangles, and volumetric extensions of them. This software allows producing complex phantoms using geometric shapes and their combinations.[32]

In our realistic breast phantom design, we created the many anatomical structures and combinations of them adapting some geometrical objects offered by TomoPhantom software to mimic complex breast anatomy. TomoPhantom software creates the objects by defining the unitless parameter of user inputs such as the x-y-z positions (range in $[-1, 1]$), diameters (range in $[0, 2]$), and rotation angles (range in $[0, 180]$) in 3 axes and intensity values (range in $[0, 1]$). The basic object name, eg, ellipsoid, cuboid, and phantom dimension, eg, 64-512 are also defined in the software by the user. Therefore, our realistic breast phantom was generated unitless dimension-based. The objects selected to create the complex breast phantom and their name of structure and number of objects are given in Table 1, and the basic versions of them are shown in Figure 1. Many structures mimicking the main parts of real breast anatomy including the nipple, milk ducts, lobules (glandular tissue), ribs, and chest wall were created in the phantom via TomoPhantom software. Due to the incapability of very small size object generation via TomoPhantom, the microcalcifications with one-pixel size in the breast were generated using a separate MATLAB code. The phantoms of different sizes ranging from 64^3 to 512^3 were created and microcalcifications were embedded in the central slice of the phantom as 4 groups of 4 each, eg, in the 128th layer of 256^3 model. The various intensities were assigned for all objects to create a contrast between the anatomical structures, and the simulated ratio of glandular/adipose tissue was produced as 3.4765%. Adipose tissue was assumed as the rest of the glandular tissue, ribs, and chest wall of the phantom.

Simultaneous Algebraic Reconstruction Technique (SART)

The SART, which can capture great details of the objects with only a few projections, has been widely used in medical image reconstructions after introducing by Anderson and Kak in 1984.[9] SART is a superior implementation of the ART introduced by Kaczmarz in 1937,[8] which focuses on finding a solution iteratively to a linear algebraic problem. The imaging system of the DBT can be modeled as a formulation in equation

Table 1. The description of realistic breast phantom.

Name of structure	Name of geometric objects	No. of objects
Breast tissue	Ellipsoid	1
Chest wall	Cuboid	1
Nipple	Ellipsoid	1
Lobules	Ellipsoid	48
Milk ducts	Cuboid	19
Ribs	Ellipsoid	50
Microcalcifications	Generated using a separate MATLAB code	16

(1) which is an ill-posed linear inverse problem.

$$A_{nxm} \bullet \vec{X}_{mx1} = \vec{Y}_{nx1} \quad (1)$$

In the equation, $A_{nxm} \in R^{nm}$ is an nxm size system matrix of the measurement that includes the voxel indices and the intersection lengths of the voxels by the ray. $\vec{X}_{mx1} \in R^m$ is an $mx1$ size column vector that includes the voxel values of the reconstructed 3D image of the target, $\vec{Y}_{nx1} \in R^n$ is an $nx1$ size column vector containing the pixel values of the projection acquired from the target at an angle. All individual elements of A_{nxm}, a_{ij} refers to the contribution of the jth voxel of the target object to the ith x-ray. To explain with the equation, the purpose of the DBT imaging modality is to obtain $\vec{X}_{mx1}$ from $\vec{Y}_{nx1}$ using measurement system matrix A_{nxm} and applying the image reconstruction method. The Landweber iteration[35] is an algorithm of finding one least squares solution for (1) among all possible solutions, especially for ill-posed linear inverse problems that involve constraints in image reconstruction.[16,36,37] SART, which is a special case of the Landweber iteration provides an iterative solution for equation (1) as formulated in equation (2).

$$X_j^{(t+1)} = X_j^{(t)} + \frac{\lambda_t}{\sum_{i=1}^{N} a_{ij}} \sum_{i=1}^{N} \left[\frac{Y_i - \sum_{m=1}^{M} a_{im} X_m^{(t)}}{\sum_{m=1}^{M} a_{im}} \right] \cdot a_{ij} \quad (2)$$

In equation (2), λ_t is a relaxation parameter and chosen by considering the convergence theorem.[38] t is the number of the iteration and can be determined empirically. We reconstructed the 3D images of the 256^3-size phantom using FBP and SART modules of LAVI reconstruction tool. We performed both FBP and SART (with 1, 2, 4, 8 iterations) for 11, 15, 19, and 23 projections.
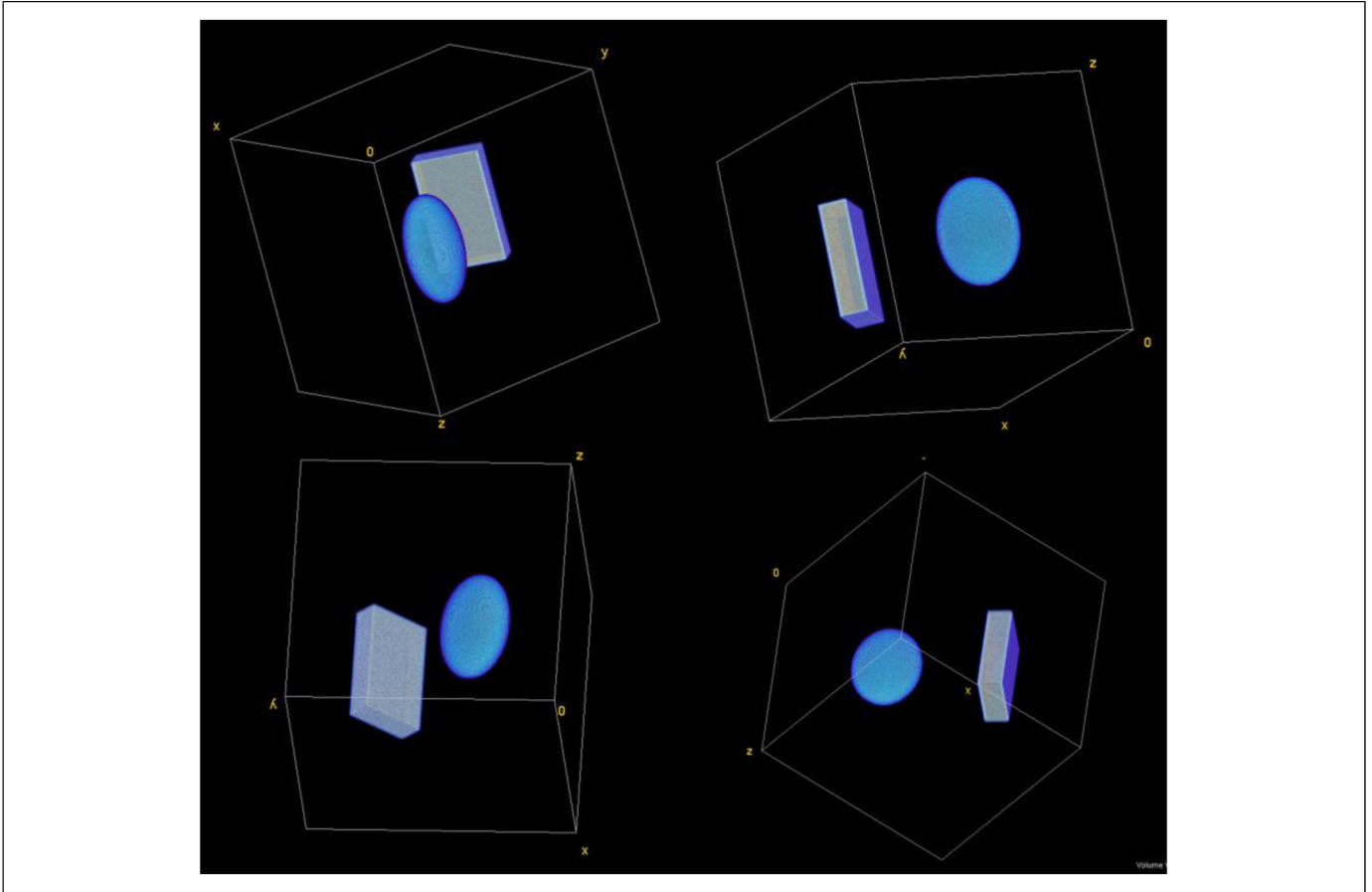
Finally, we compared the outputs of the reconstructed images by FBP and SART quantitatively and qualitatively. We enlarged the views of embedded microcalcifications to increase the visibility in the original phantom in Figure 2. For qualitative analysis, after reconstructions, we checked the visibility of microcalcifications comparing the images of the original layer of interest (LOI), FBP, and SART (Figures 3 and 4), respectively. For quantitative analysis, we utilized the metrics; the contrast-to-noise ratio (CNR) (see equation (3)),[39,40] full width half maximum (FWHM), and 1D profile. FWHM is defined as 2355 times the standard deviation along a line (2355σ), whereas 1D profile expresses the tendency of the change of the pixel values along a line. For this purpose, we described the region of interest (ROI), the background of the ROI, the FWHM line, and the 1D profile line in the LOI as shown in Figure 3(a) for both original and reconstructed images.

$$CNR = \frac{\mu_{ROI} - \mu_{background}}{\sigma_{background}} \quad (3)$$

In equation (3), $\sigma_{background}$ is the standard deviation of the background, μ_{ROI} and $\mu_{background}$ are the mean values of the ROI and background, respectively.

Figure 1. The various perspectives of the visualization of the three-dimensional (3D) volume of basic objects (eg cuboid and ellipsoid) used in the realistic breast phantom design.

Results

The realistic breast phantom that ranges from 64^3 to 512^3 in dimensions including the anatomical structures and microcalcifications was created successfully and made eligible for reconstruction. The visualization of a 3D volume of realistic breast phantom with sizes 64^3, 128^3, 256^3, and 512^3 in various styles, and the enlarged views of microcalcifications (4×4 set) are given in Figure 2. The ratio of glandular/adipose tissue of the phantom was calculated as 3.4765%. The creating times of our proposed realistic breast phantom for 64^3, 128^3, 256^3, and 512^3 were 2.5916 s, 8.4626 s, 57.6858 s, and 472.1734 s, respectively. These computation times were performed with a workstation that has 11th Gen Intel(R) Core(TM) i9-11900H @ 2.50 GHz, 16 cores, 32 GB RAM, and 16 GB NVIDIA GeForce RTX 3080. The reconstructed images of the 256^3 size phantom as 256 slices in the longitudinal axis were obtained by FBP and SART modules of LAVI and compared qualitatively and quantitatively. The center slice, 128th layer, of the phantom that includes the microcalcifications was chosen as the LOI. The comparisons of the original LOI, the reconstructed LOI via FBP, and the reconstructed LOI via SART are given in Figure 3(a), (b), and (c), respectively. The iteration number of SART was 1 and the projection numbers of both FBP and SART were 11.

In Figure 3, for qualitative analysis, we focused on the top set of 4-microcalcification and enlarged a frame at 2 levels with the 1000% magnification ratio. For quantitative analysis, we determined the 4-microcalcifications as the ROI and surrounding them in the frame as the background to calculate the CNR values of the LOI of the original, FBP, and SART. Additionally, we defined an FWHM line to its element below the 4-microcalcification group and a 1D profile line that intersects the middle-left and -right members of the group. To evaluate qualitatively, as a result of FBP and SART (1 iteration) obtained with 11 projections, microcalcifications could be reconstructed. However, to analyze which method is better quantitatively, reconstruction results applied with the increased number of projections and iterations is discussed below. We presented the enlarged views of the top 2 groups of 4-microcalcification set for original LOI, FBP, SART (1 iter.), SART (2 iter.), SART (4 iter.), and SART (8 iter.) for 11, 15, 19, and 23 projections in Figure 4. In the quantitative assessment in Figure 5, we demonstrated the comparison of the CNR values for all reconstruction methods with the determined iteration and projection numbers. We also presented the more quantitative analysis of reconstructed images applying the FWHM metric in Figure 6 and applying the 1D profile metric in Figure 7, respectively.
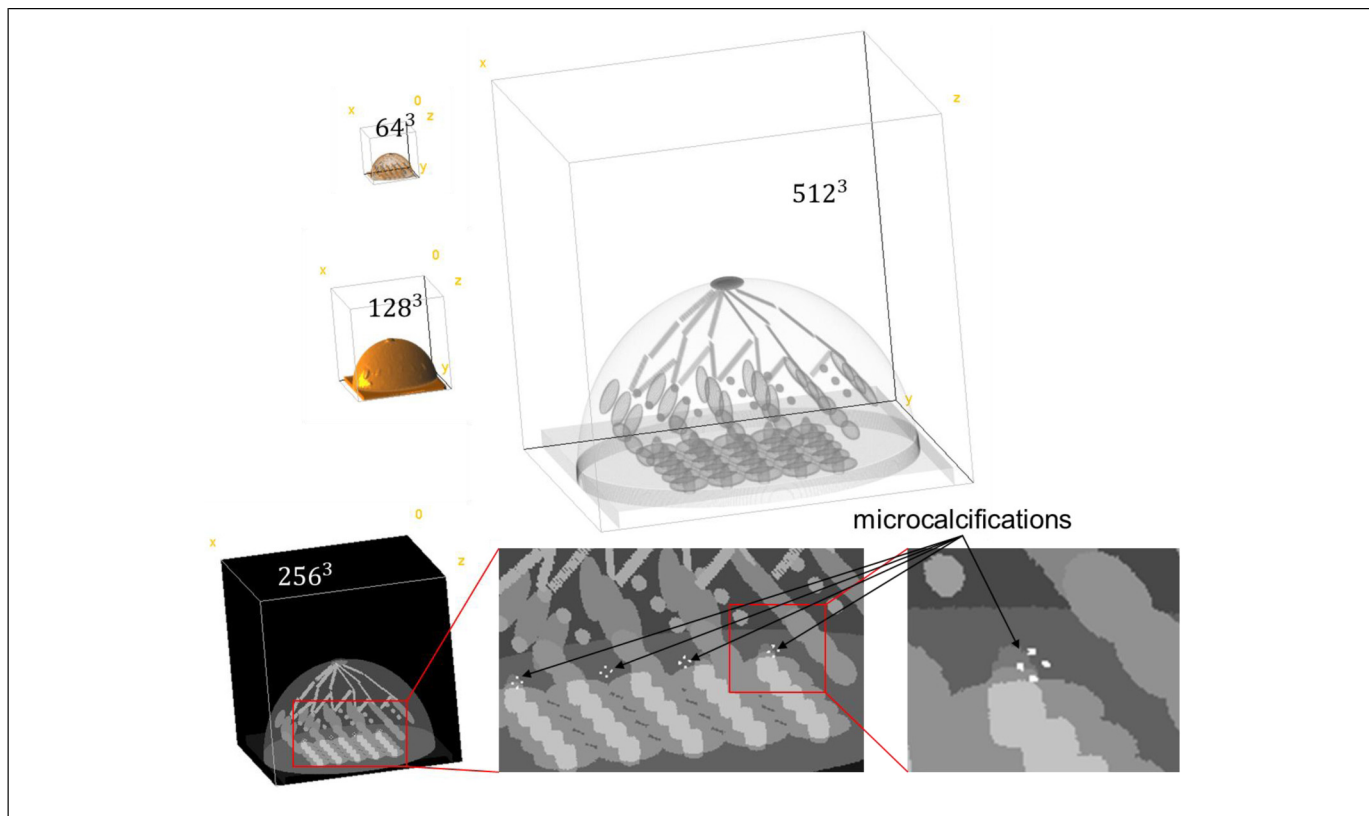
Figure 2. The visualization of the three-dimensional (3D) volume of breast for the dimensions of 64^3, 128^3, 256^3, and 512^3; the enlarged views of microcalcifications.
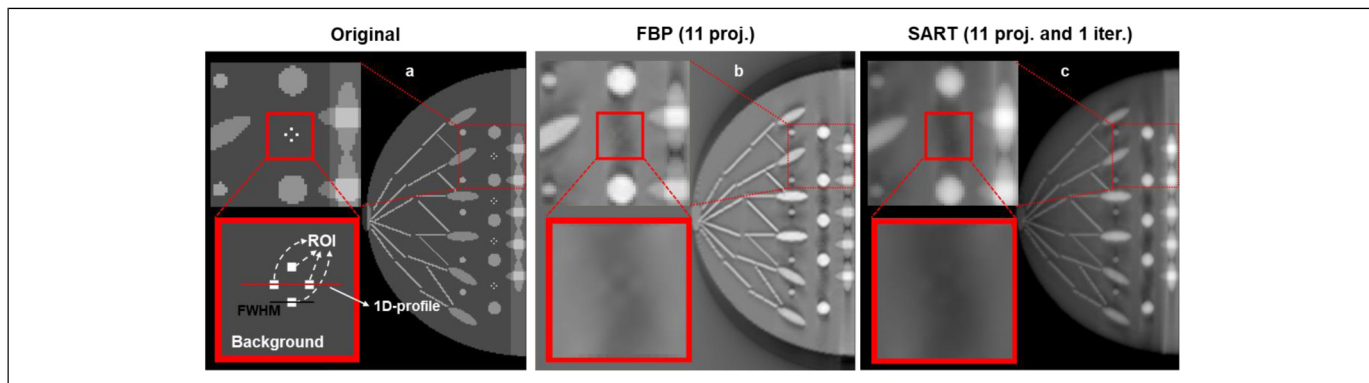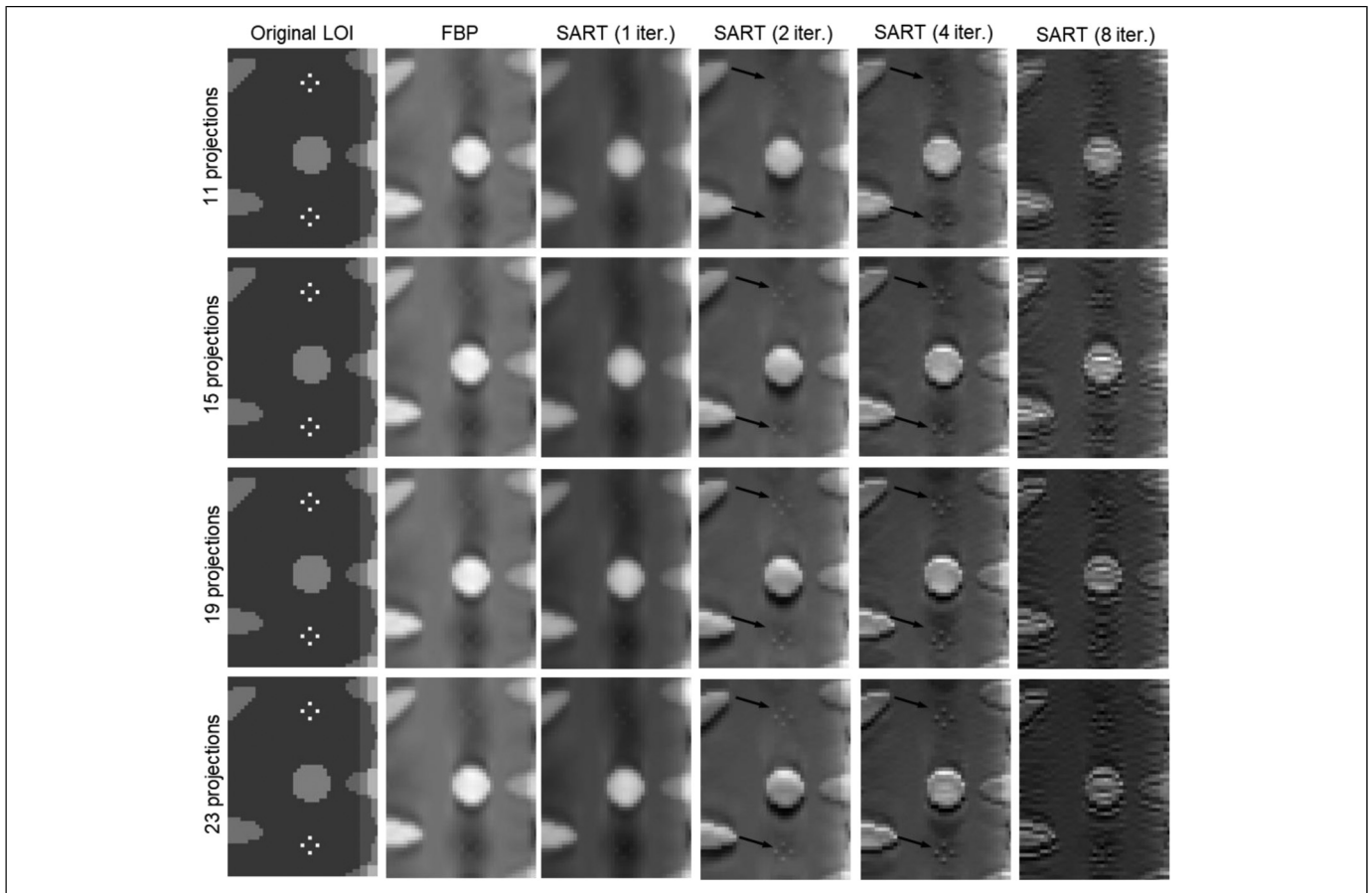

Figure 3. The comparison of the original layer of interest (LOI) (128th slice) (a), the reconstructions of LOI via filtered back projection (FBP) (b), and simultaneous algebraic reconstruction technique (SART) (1 iteration) (c) for 11 projections. (a) The description of region of interest (ROI), background of ROI, full width half maximum (FWHM) line, and 1D profile line.
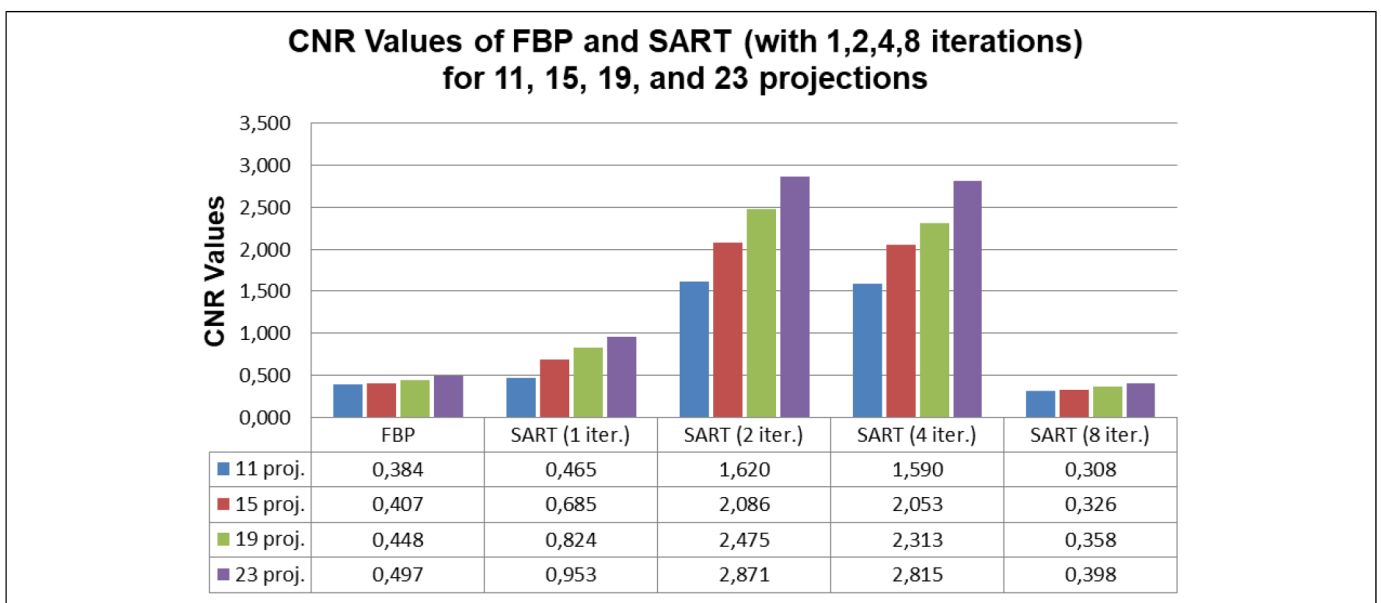
Discussions

The meticulousness of the phantom design was that the microcalcifications were very small compared to the size of the breast as they really are hidden in only 1 layer and they can be captured with FBP and SART. The generation time of the realistic phantom, which is less than 8 min for 512^3, is pretty feasible to examine the different reconstruction algorithms easily and quickly. This provides an opportunity for various revisions on the realistic breast phantom. The phantom has some limitations such as the inability to express dimensions in metrics and the lack of real x-ray attenuation values of breast tissue.
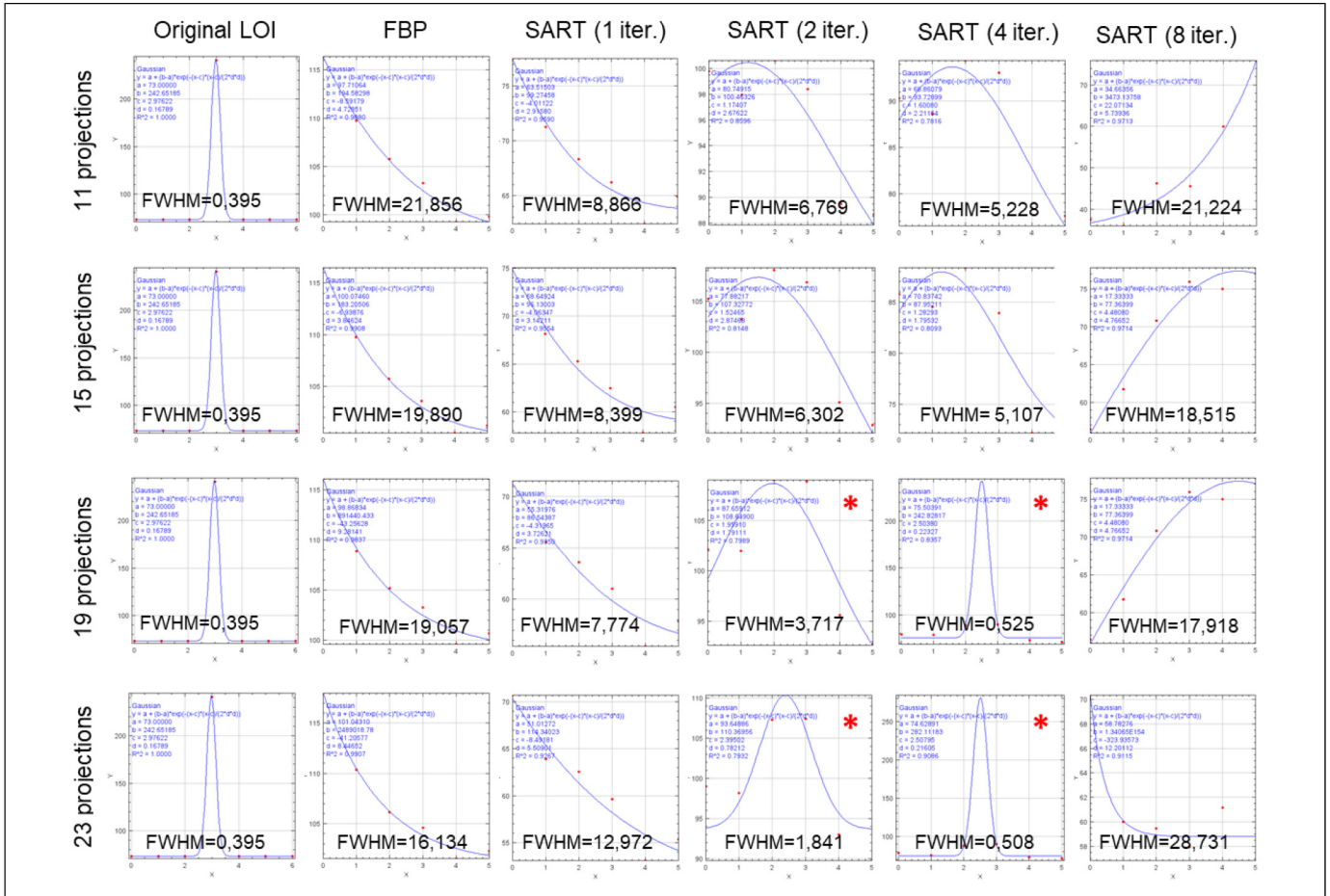
According to the comparison of the reconstructed images, SART (2 iter.) and SART (4 iter.) yields the best visibility of the microcalcifications (pointed with black arrows on the

Figure 4. The comparison of enlarged views of regions of interest (ROIs) of the reconstructed images via filtered back projection (FBP) and simultaneous algebraic reconstruction technique (SART) (1-2-4-8 iterations) for 11, 15, 19, and 23 projections.

	FBP	SART (1 iter.)	SART (2 iter.)	SART (4 iter.)	SART (8 iter.)
■ 11 proj.	0,384	0,465	1,620	1,590	0,308
■ 15 proj.	0,407	0,685	2,086	2,053	0,326
■ 19 proj.	0,448	0,824	2,475	2,313	0,358
■ 23 proj.	0,497	0,953	2,871	2,815	0,398

Figure 5. The comparison of the contrast-to-noise ratio (CNR) values of the regions of interest (ROIs) of the reconstructed images via filtered back projection (FBP) and simultaneous algebraic reconstruction technique (SART) (1-2-4-8 iterations) for 11, 15, 19, and 23 projections.
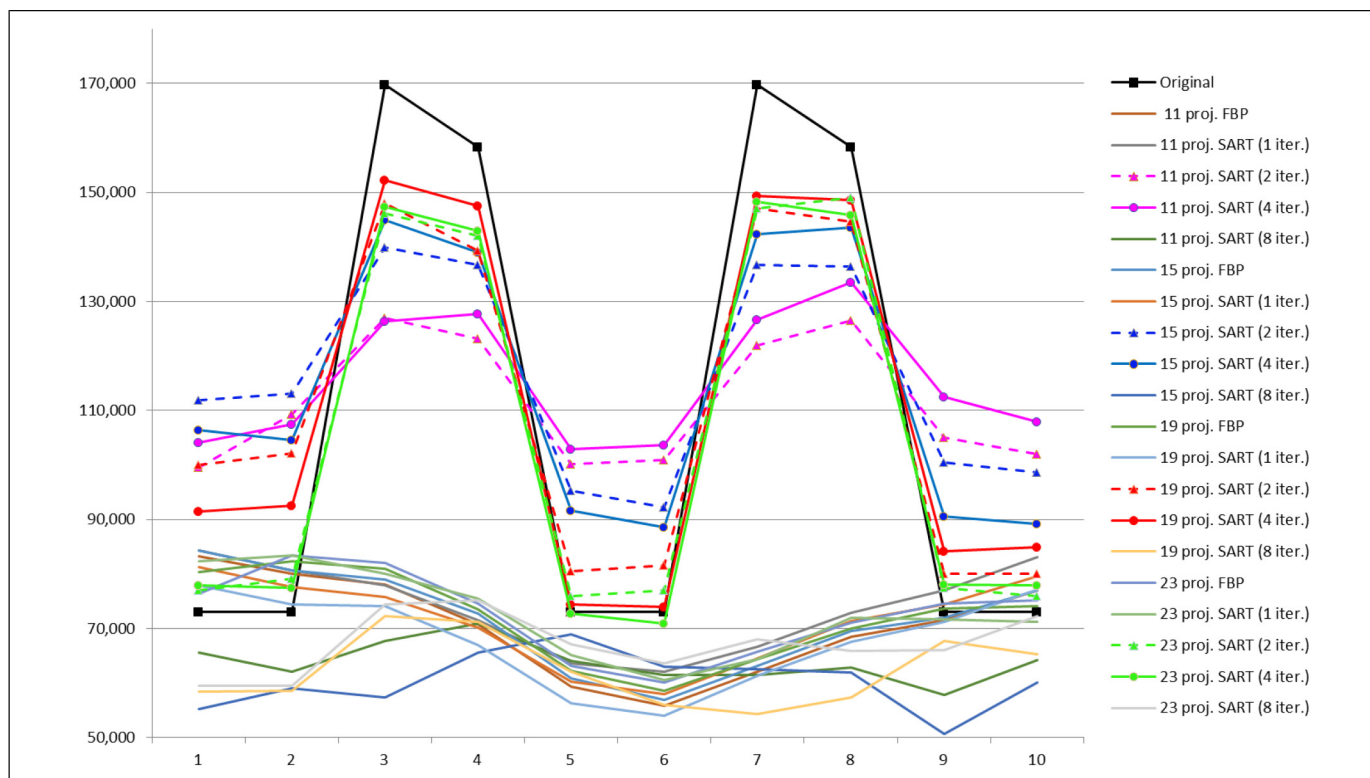
Figure 6. The comparison of the full width half maximum (FWHM) of the reconstructed images via filtered back projection (FBP) and simultaneous algebraic reconstruction technique (SART) (1-2-4-8 iterations) for 11, 15, 19, and 23 projections.

images) for all numbers of the projections. It is clear that increasing the number of the iteration to 8 in SART causes distortion of the images. The reconstructed images by FBP and SART (1 iter.) yield very close results in the manner of visibility of the microcalcifications, but they are not as clear as the reconstructed images by SART (2,4 iter.) (Figure 4). These qualitative evaluations are also supported by the values of the CNR, which is the first metric used for quantitative analysis. The CNR values of SART (2 iter.) and SART (4 iter.) are very close to each other and they are also much higher than the CNR values of FBP, SART (1 iter.), and SART (8 iter.). Besides, when the CNR graph is examined, it is very clear that increasing the number of projections increases the CNR values as expected. For example, while CNR values of SART (2 iter.) for 11 and 23 projections were calculated, respectively, 1.620 and 2.871, the CNR values of FBP were calculated as 0.384 and 0.497 for the same projection numbers (Figure 5).

The value of FWHM of original LOI was 0.395 and its characterization looks like an impulse which indicates the best resolution to distinguish the elements of the microcalcifications. The closest results to this FWHM character of

the original LOI were obtained with SART (2 iter.) and SART (4 iter.) methods applied with 19 and 23 projections marked with a red asterisk in Figure 6. Among these 4 results, the best FWHM with the value of 0.508 was obtained SART (4 iter.) method applied with 23 projections.

In Figure 7, when the 1D-profile tendency is examined, the closest behavior to the original LOI profile behavior (black solid line) was shown by the reconstructed images obtained with 19 (red) and 23 (green) projections SART (2 iter.) (dash line) and SART (4 iter.) (solid line). Considering the results of FWHM, 1D profile, and CNR metric in general, SART (2), and SART (4) methods with 11 and 15 projections also provided images with acceptable quality. According to the overall qualitative and quantitative evaluation of the reconstructed images obtained from all methods applied with all projections, FBP and SART (1 iter.) captured the microcalcifications slightly, while SART (8 iter.) gave completely distorted results. On the other hand, for all projections, SART (2 iter.) and SART (4 iter.) were able to successfully capture microcalcifications with significant results.

Figure 7. The comparison of the 1D profiles of the reconstructed images via filtered back projection (FBP) and simultaneous algebraic reconstruction technique (SART) (1-2-4-8 iterations) for 11, 15, 19, and 23 projections.

Conclusions

In this study, we created and proposed a realistic breast phantom that mimics the structures in a real breast such as the nipple, lobules, ribs, milk ducts, chest wall, and also includes the microcalcifications. We tested the performance of iterative (SART) and analytical (FBP) image reconstruction methods with various parameters such as the number of projections (11-23) and iterations (1-8 for SART) applying to this realistic breast phantom. In this way, it was possible to analyze the effects of the selection of reconstruction methods before clinical applications of DBT and to control its parameters. We proved that a computationally efficient realistic breast phantom can be used for pretest purposes in DBT in terms of establishing the basis for clinical applications. In future work, with the development of the phantom that has more sophisticated breast tissue modeling and applying the appropriate parameters of reconstruction in the clinic, overdose radiation of patients will be prevented.

Declaration of Conflicting Interests

The author(s) declared no potential conflicts of interest with respect to the research, authorship, and/or publication of this article.

Funding

ORCID iDs

Adem Polat 🔟 https://orcid.org/0000-0002-5662-4141
Raziye Kubra Kumrular 🔟 https://orcid.org/0000-0002-0976-3683

References

1. Henrot P, Leroux A, Barlier C, Génin P. Breast microcalcifications: the lesions in anatomical pathology. *Diagn Interv Imaging*. 2014;95(2):141-152.
2. Wang J, Yang X, Cai H, Tan W, Jin C, Li L. Discrimination of breast cancer with microcalcifications on mammography by deep learning. *Sci Rep*. 2016;6(1):1-9.
3. Kopans DB, Meyer JE, Sadowsky N. Breast imaging. *N Engl J Med*. 1984;310(15):960-967.
4. Niklason LT, Christian BT, Niklason LE, et al. Digital tomosynthesis in breast imaging. *Radiology*. 1997;205(2):399-406.
5. Helvie MA. Digital mammography imaging: breast tomosynthesis and advanced applications. *Radiol Clin*. 2010;48(5):917-929.
6. Wu T, Moore RH, Rafferty EA, Kopans DB. A comparison of reconstruction algorithms for breast tomosynthesis. *Med Phys*. 2004;31(9):2636-2647.
7. Levakhina Y. *Three-Dimensional Digital Tomosynthesis: Iterative Reconstruction, Artifact Reduction and Alternative Acquisition Geometry*. Springer; 2014.

8. Kaczmarz S. Approximate solution of systems of linear equations. *Bull Int Acad Pol Sci Lettt A*. 1937;35:355-357.

9. Andersen AH, Kak AC. Simultaneous algebraic reconstruction technique (SART): a superior implementation of the ART algorithm. *Ultrason Imaging*. 1984;6(1):81-94.

10. Bracewell RN, Riddle A. Inversion of fan-beam scans in radio astronomy. *Astrophys J*. 1967;150:427.

11. Ramachandran GN, Lakshminarayanan AV. Three-dimensional reconstruction from radiographs and electron micrographs: application of convolutions instead of Fourier transforms. *Proc Natl Acad Sci*. 1971;68(9):2236-2240.

12. Kak AC, Slaney M, Wang G. *Principles of Computerized Tomographic Imaging*. Wiley Online Library; 2002.

13. Shepp LA, Logan BF. The Fourier reconstruction of a head section. *IEEE Trans Nucl Sci*. 1974;21(3):21-43.

14. Ekstrom MP. *Digital Image Processing Techniques*, Vol. 2. Academic Press; 2012.

15. Radon J. On the determination of functions from their integrals along certain manifolds. *Ber Verh, Sachs Akad Wiss*. 1917;69:262-277.

16. Ji D, Qu G, Liu B. Simultaneous algebraic reconstruction technique based on guided image filtering. *Opt Express*. 2016;24(14):15897-15911.

17. Flores L, Vidal V, Verdú G. Iterative reconstruction from few-view projections. *Procedia Comput Sci*. 2015;51:703-712.

18. Myers GR, Paganin DM, Gureyev TE, Mayo SC. Phase-contrast tomography of single-material objects from few projections. *Opt Express*. 2008;16(2):908-919.

19. Myers GR, Gureyev TE, Paganin DM, Mayo SC. The binary dissector: phase contrast tomography of two-and three-material objects from few projections. *Opt Express*. 2008;16(14):10736-10749.

20. Myers GR, Thomas CDL, Paganin DM, Gureyev TE, Clement JG. A general few-projection method for tomographic reconstruction of samples consisting of several distinct materials. *Appl Phys Lett*. 2010;96(2):21105.

21. Sidky EY, Kao C-M, Pan X. Accurate image reconstruction from few-views and limited-angle data in divergent-beam CT. *J Xray Sci Technol*. 2006;14(2):119-139.

22. Vimieiro RB, Borges LR, Vieira MAC. Open-source reconstruction toolbox for digital breast tomosynthesis. In: XXVI Brazilian congress on biomedical engineering, 2019, pp.349-354.

23. Vimieiro RB, Borges LR, Caron RF, et al. Noise measurements from reconstructed digital breast tomosynthesis. *Medical Imaging 2019: Physics of Medical Imaging*. 2019;10948:74-85.

24. Bakic PR, Barufaldi B, Higginbotham D, et al. Virtual clinical trial of lesion detection in digital mammography and digital breast tomosynthesis. *Medical Imaging 2018: Physics of Medical Imaging*. 2018;10573:1057306.

25. Barufaldi B, Higginbotham D, Bakic PR, Maidment ADA. OpenVCT: a GPU-accelerated virtual clinical trial pipeline for mammography and digital breast tomosynthesis. *Medical Imaging 2018: Physics of Medical Imaging*. 2018;10573:1057358.

26. Scarparo DC, Salvadeo DHP, Pedronette DCG, Barufaldi B, Maidment ADA. Evaluation of denoising digital breast tomosynthesis data in both projection and image domains and a study of noise model on digital breast tomosynthesis image domain. *J Med Imaging*. 2019;6(3):31410.

27. Van Aarle W, Palenstijn WJ, De Beenhouwer J, et al. The ASTRA toolbox: a platform for advanced algorithm development in electron tomography. *Ultramicroscopy*. 2015;157:35-47.

28. Van Aarle W, Palenstijn WJ, Cant J, et al. Fast and flexible X-ray tomography using the ASTRA toolbox. *Opt Express*. 2016;24-(22):25129-25147.

29. Ching DJ, Gürsoy D. XDesign: an open-source software package for designing x-ray imaging phantoms and experiments. *J Synchrotron Radiat*. 2017;24(2):537-544.

30. Gürsoy D, De Carlo F, Xiao X, Jacobsen C. Tomopy: a framework for the analysis of synchrotron tomographic data. *J Synchrotron Radiat*. 2014;21(5):1188-1193.

31. Faragó T, Mikulík P, Ershov A, Vogelgesang M, Hänschke D, Baumbach T. Syris: a flexible and efficient framework for X-ray imaging experiments simulation. *J Synchrotron Radiat*. 2017;24(6):1283-1295.

32. Kazantsev D, Pickalov V, Nagella S, Pasca E, Withers PJ. Tomophantom, a software package to generate 2D–4D analytical phantoms for CT image reconstruction algorithm benchmarks. *SoftwareX*. 2018;7:150-155.

33. Glick SJ, Ikejimba LC. Advances in digital and physical anthropomorphic breast phantoms for x-ray imaging. *Med Phys*. 2018;45(10):e870-e885.

34. Bakic PR, Zhang C, Maidment ADA. Development and characterization of an anthropomorphic breast software phantom based upon region-growing algorithm. *Med Phys*. 2011;38-(6Part1):3165-3176.

35. Landweber L. An iteration formula for Fredholm integral equations of the first kind. *Am J Math*. 1951;73(3):615-624.

36. Bauschke HH, Burachik RS, Combettes PL, Elser V, Luke DR, Wolkowicz H. *Fixed-point Algorithms for Inverse Problems in Science and Engineering*, Vol. 49. Springer Science & Business Media; 2011.

37. Qu G, Wang C, Jiang M. Necessary and sufficient convergence conditions for algebraic image reconstruction algorithms. *IEEE Trans Image Process*. 2008;18(2):435-440.

38. Censor Y, Elfving T, Herman GT, Nikazad T. On diagonally relaxed orthogonal projection methods. *SIAM J Sci Comput*. 2008;30(1):473-504.

39. Polat A, Yildirim I. An iterative reconstruction algorithm for digital breast tomosynthesis imaging using real data at three radiation doses. *J Xray Sci Technol*. 2018;26(3):347-360.

40. Polat A, Matela N, Dinler A, Zhang YS, Yildirim I. Digital breast tomosynthesis imaging using compressed sensing based reconstruction for 10 radiation doses real data. *Biomed Signal Process Control*. 2019;48:26-34.